Journal of Fluids and Structures 138 (2025) 104392

Contents lists available at ScienceDirect

Journal of Fluids and Structures

journal homepage: www.elsevier.com/locate/jfs

Mitigating unsteady loads at low Reynolds numbers using a passive trailing-edge flap

C. Martínez-Muriel [a], I.M. Viola [b], M. García-Villalba [c], O. Flores [a,*]

[a] Aerospace Engineering Department, Universidad Carlos III de Madrid, Spain
[b] School of Engineering, Institute for Energy Systems, University of Edinburgh, Edinburgh, EH9 3FB, UK
[c] Institute of Fluid Mechanics and Heat Transfer, TU Wien, Vienna, Austria

ARTICLE INFO

Keywords:
Unsteady aerodynamics
Unsteady load mitigation
Passive trailing-edge flap
Bioinspired robotic vehicles
Micro drones
Micro autonomous underwater vehicles

ABSTRACT

The load mitigation potential of a passive pitching trailing edge flap for NACA0012 airfoils at a Reynolds number of 1000 subjected to oscillations in the angle of attack is analyzed. For this purpose, direct numerical simulations of the two-dimensional, incompressible flow have been conducted to examine the effectiveness of the flap in reducing aerodynamic load fluctuations across a range of oscillation amplitudes and flap-to-chord ratios. The validity of a quasi-steady model to predict the load mitigation using passive pitching flaps, previously proposed in the literature and predicting a load mitigation proportional to the flap-to-chord length ratio, a/c, is here investigated for large amplitude oscillations. The results show that the increment in the reduction in fluctuations is generally proportional to the increment in a/c. This closely aligns with the predictions of the quasi-steady theory, even for the cases with the largest oscillation amplitudes, where non-linear aerodynamic effects are present, although some variation is observed. Notably, we explored the interaction between vortical structures and the flap dynamics, and its relevance on the flow patterns around the airfoil and ultimately on load mitigation. This interaction, alongside flap inertia, provides insight into the timing and magnitude of load reduction, demonstrating the potential of tailored passive pitching mechanisms for unsteady flow conditions. These findings offer valuable insights for the design and development of passive unsteady load mechanisms for small aerial and underwater vehicles, as well as microscale energy harvesters, by highlighting the relevance of considering non-linear effects in their optimization.

1. Introduction

Unsteady aerodynamic loads are a critical concern in numerous engineering applications featuring lifting surfaces, as they can cause structural failure, fatigue, performance degradation, and increased control effort. These loads are particularly relevant in systems subject to cyclic or transient aerodynamic disturbances, such as wind turbines and aircraft. For instance, both horizontal-axis and vertical-axis wind turbines experience periodic loading due to atmospheric turbulence and rotational effects, leading to fatigue-driven maintenance and lifespan limitations (Han et al., 2016). Similarly, aircraft are routinely exposed to atmospheric gusts and turbulence that can induce rapid, high-magnitude force fluctuations on lifting surfaces, requiring robust load control strategies to maintain structural integrity and flight safety (Jones et al., 2022).

* Corresponding author.
E-mail address: oflores@ing.uc3m.es (O. Flores).

https://doi.org/10.1016/j.jfluidstructs.2025.104392
Received 10 December 2024; Received in revised form 3 June 2025; Accepted 24 July 2025
Available online 21 August 2025

A crucial parameter in analyzing unsteady aerodynamic loads is the Reynolds number, Re, usually defined in terms of the free-stream velocity, the airfoil chord and the fluid viscosity. This non-dimensional number governs the relative importance of inertial to viscous forces in the flow. At high Reynolds numbers, common in large wind turbines and commercial aircraft, the flow tends to remain largely attached, and linearized potential flow theory offers analytical insights into lift and load behavior. This approximation was used in the pioneering works of Theodorsen (1935), Garrick (1936) and Theodorsen and Garrick (1942) to characterize lift and drag on sinusoidally oscillating airfoils, laying the foundations of unsteady potential flow theory. This theoretical framework continues to evolve, with ongoing research revisiting and refining these established models (Fernandez-Feria, 2016, 2017; Alaminos-Quesada, 2021), providing a solid foundation for the design of load mitigation strategies at high Reynolds numbers.

In contrast to the attached flows in potential aerodynamics, low-Reynolds number flows are dominated by viscous and non-linear effects: boundary layer separation, formation of leading edge vortices (LEV) (Eldredge and Jones, 2019) and vortex shedding (Bose and Sarkar, 2018). These inherently nonlinear phenomena introduce significant complexity in the prediction of unsteady loads, for instance during the recovery phase of a gust encounter (Martínez-Muriel and Flores, 2020; Moriche et al., 2021), which hinders the development of efficient mitigation strategies.

To manage such loads, both active and passive control strategies have been developed. Active methods use sensors, actuators and control systems (Johnson et al., 2010) to adjust the aerodynamic profile in real time. These methods include pitch adjustment in wind turbine blades (Navalkar et al., 2016), or the activation of control surfaces in wind turbines (Bottasso et al., 2016b) and aircraft (Moulin and Karpel, 2007). However, they come at the cost of increased system complexity, weight, and energy consumption, which can undermine their effectiveness for some applications (Lackner and van Kuik, 2010).

In contrast, passive methods require no external energy input or active feedback, offering simpler and potentially more robust solutions. Prior research has demonstrated the effectiveness of passive mechanisms at high Reynolds numbers, showing comparable performance as active systems with reduced complexity. For instance, in the context of wind turbines, recent work has demonstrated the load alleviation capabilities of passive trailing edge flaps (Bottasso et al., 2016a) and articulated tip devices (Bottasso et al., 2016b). Notably, Arredondo-Galeana et al. (2021) proposed a quasi-steady linear model for load mitigation using a passive trailing edge flap, validated through experiments at $Re = 50{,}000$. Their results suggest that passive flaps reduce unsteady loads with an effectiveness that scales linearly with the flap-to-chord ratio.

Despite this progress, the applicability of such passive devices in low-Re regimes remains largely unexplored. Biological swimming and flying provide some encouraging results, given that the flexibility of wings and fins is a well-known contributor to stabilize and enhance the flight of birds, insects, and the swimming of fish (Marais et al., 2012; Senda et al., 2012; Addo-Akoto et al., 2021). However, there is a need for detailed investigations that go beyond linear theory to understand how passive flaps perform under these nonlinear conditions. In particular, it is critical to analyze the underlying flow physics to determine the mechanisms of load mitigation and to identify how flap geometry and kinematics influence performance.

The objective of this study is to characterize the performance of a passive TE flap in the load mitigation of an airfoil at low-Reynolds numbers, extending the parametric space of Reynolds number, flap dimensions and forcing kinematics beyond what has been studied in the literature. Specifically, we aim to evaluate when and how non-linear effects (boundary layer separation and/or LEV formation) become relevant for the load-mitigation capability of the passive flap. The study also aims at assessing how can these effects be taken into account into the preliminary design of passive flaps, including an evaluation of the predictive capabilities of the QS model of Arredondo-Galeana et al. (2021) at the low-Re regime considered here.

To achieve these goals, we perform direct numerical simulations of the 2D incompressible flow around airfoils incorporating passive-pitching trailing edge flaps at $Re = 1000$. The simulations span a wide range of reduced frequencies, heaving amplitudes, and flap lengths to explore flow-flap interactions across different dynamic regimes. Note that the selected value of the Reynolds number is representative of the operating condition of small-scale bioinspired devices, like microscale wind turbines (Holden et al., 2015; Gaitan-Aroca et al., 2020) or micro-air-vehicles (De Croon et al., 2009; Roshanbin et al., 2017; Folkertsma et al., 2017), where viscous effects and flow separation are prominent.

This paper is organized as follows: Section 2 introduces the problem setup and the numerical methodology used to solve the coupled fluid–structure interaction. Section 3 presents the simulation results, analyzing the aerodynamic response, flap dynamics, and flow structures involved in load mitigation. The applicability of the QS model is also examined. Finally, Section 4 summarizes the key findings and outlines potential directions for future work.

2. Methodology

2.1. Problem definition

The problem of load mitigation on a NACA0012 airfoil subjected to oscillations in the angle of attack is considered here. First, let us consider a rigid NACA0012 airfoil of chord c immersed in a uniform free stream of intensity U_∞, see Fig. 1a. We consider low Mach numbers so that we can assume that the flow is incompressible. The fluid is considered to be Newtonian with constant density ρ and dynamic viscosity μ. We fix the Reynolds number to be $Re = \rho U_\infty c/\mu = 1000$. The airfoil is initially set at a given angle of attack α.

To model the disturbances of a gusty environment, we introduce oscillations in the effective angle of attack of the airfoil with amplitude α_0'. Following previous work on sine-squared gusts (Perrotta and Jones, 2018; Moriche et al., 2021), we model these oscillations in the angle of attack by imposing a sinusoidal heaving motion in the airfoil,

$$h(t) = h_0 \cos(2\pi f t), \tag{1}$$

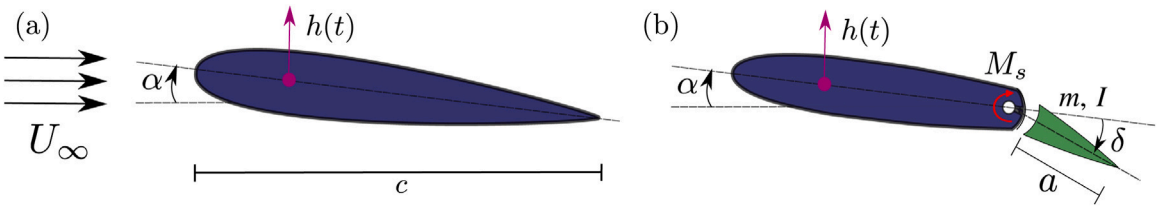

Fig. 1. (a) Sketch of a rigid airfoil immersed in a free stream. (b) Sketch of an airfoil using a passive-pitching trailing edge flap.

Table 1
Overview of the selected values for the variables defining the parametric space.

a/c	ρ_s/ρ	h_0/c	α	κ
0	1.5	0.15	0°	0.3
0.25	5	0.25	5°	0.5
0.375	25	0.5		
0.5	100			
0.75				

where h_0 is the heaving amplitude, f is the frequency of the imposed motion, and $T = f^{-1}$ is the period of oscillation. We also define the reduced frequency as $\kappa = \pi f c/U_\infty$. Note that, although the geometric angle of attack (α) is fixed, the effective angle of attack ($\alpha + \alpha'(t)$) to which the airfoil is subject varies cyclically as a result of the heaving motion. The amplitude of the oscillations in the angle of attack depend on the reduced frequency and the heaving amplitude, yielding $\alpha_0' = \tan^{-1}(2\kappa h_0/c)$. For simplicity, we choose to characterize the perturbations using κ and h_0/c.

As shown in Fig. 1b, the airfoil is equipped with a TE flap of length a. The flap deflection is measured by the angle δ, positive in the clockwise direction. The flap is characterized by a density ρ_s and a volume V that is a function of the flap length, yielding a total mass $m = \rho_s V$ and a polar moment of inertia with respect to the centroid of the flap I. The flap is connected to a very flexible linear spring with a large preload. As shown in Appendix A, these conditions yield a spring reaction that can be approximated by a constant moment M_s at the hinge. This moment is computed to ensure no flap deflection in steady conditions (i.e., $\delta = 0$ for $h_0/c = 0$), providing the same baseline steady lift and drag characteristics on the rigid and flapped airfoils. Since this is a static equilibrium condition, the density of the flap, ρ_s, does not influence the value of M_s, which only depends on the flap-to-chord length ratio a/c and on the geometric angle of attack of the airfoil, α.

In this work, different values of the flap length (a), reduced frequencies (κ), heaving amplitudes (h) and density of the flap (ρ_s) are considered. The values of the different variables are shown in Table 1.

2.2. Fluid–structure interaction solver

The fluid–structure interaction problem presented in the previous section is solved using TUCAN, a constant-density finite-difference fluid solver that uses the Immersed Boundary Method (IBM) proposed by Uhlmann (2005). The governing equations are the Navier–Stokes equations, which read

$$\nabla \cdot \boldsymbol{u} = 0, \tag{2a}$$

$$\frac{\partial \boldsymbol{u}}{\partial t} + (\boldsymbol{u}\cdot\nabla)\boldsymbol{u} = -\frac{1}{\rho}\nabla p + \nu\nabla^2\boldsymbol{u} + \boldsymbol{f}, \tag{2b}$$

$$\boldsymbol{u}(\boldsymbol{x}) = \boldsymbol{U}_{\partial\Gamma} \quad \forall \boldsymbol{x} \in \partial\Gamma, \tag{2c}$$

where $\boldsymbol{u} = (u, w)$ is the fluid velocity in the spatial field $\boldsymbol{x} = (x, z)$, t is time, ρ is the fluid density, p is the pressure, $\nu = \mu/\rho$ is the kinematic viscosity, Γ is the computational domain and $\partial\Gamma$ is its boundary. The IBM forcing term $\boldsymbol{f}$ models the presence of the airfoil, ensuring that Eq. (2)c, which is the no-slip boundary-condition, is satisfied on the contour of the airfoil.

A three-stage semi-implicit Runge–Kutta scheme is used for the temporal integration. A staggered Cartesian grid, referred here as Eulerian grid, is used to discretize the fluid, where spatial derivatives are approximated by second-order centered finite differences. The no-slip boundary condition (Eq. (2)c) is imposed on a Lagrangian grid, requiring discrete delta functions to interpolate velocities and the IBM forcing term between the Lagrangian and Eulerian grids. More details about the implementation of TUCAN can be found in Moriche (2017).

To solve for the dynamics of the flap, TUCAN is coupled to a multi-body solver (MBS). For the sake of brevity, only the relevant aspects of the MBS are described here. The governing equations of a general multi-body system can be stated as

$$H(\boldsymbol{q})\ddot{\boldsymbol{q}} + C(\boldsymbol{q}, \dot{\boldsymbol{q}}) = \boldsymbol{\xi} + \boldsymbol{\xi}_h, \tag{3}$$

where H is the generalized inertia matrix, $\boldsymbol{q}$, $\dot{\boldsymbol{q}}$ and $\ddot{\boldsymbol{q}}$ are the vector of generalized coordinates and its first and second time derivatives, where $\boldsymbol{q} = [\alpha, h, \delta]$ for this particular problem, C is the generalized bias force vector, accounting for Coriolis and

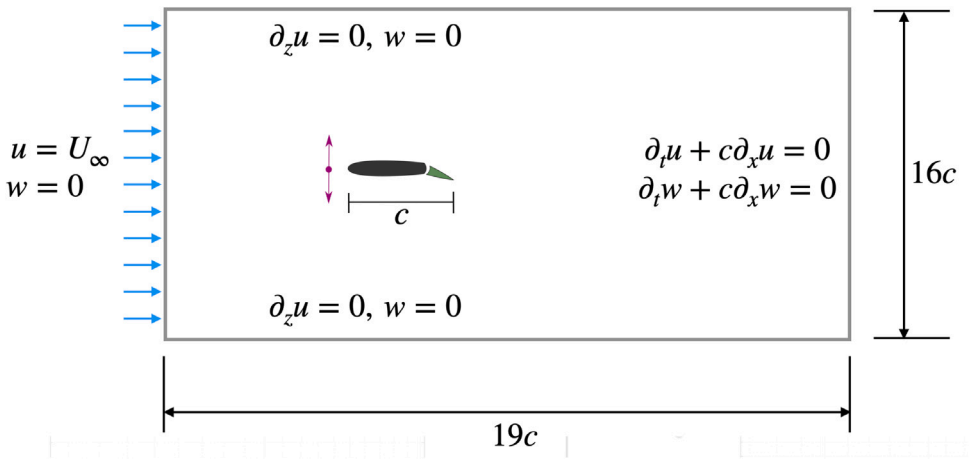

Fig. 2. Sketch of the computational set-up and selected boundary conditions.

centrifugal accelerations, $\boldsymbol{\xi} = [0, 0, M_s]$, where M_s is the constant moment applied at the hinge, and $\boldsymbol{\xi}_h$ is the vector of hydrodynamic forces acting on the airfoil. The effect of the gravity is not considered in this work. The open-source Rigid Body Dynamics Library (RBDL) developed by Felis (2017) is used to compute the matrices H and C.

TUCAN and the MBS are *weakly* coupled, posing a limit on the solid-to-fluid density ratio, $\rho^* = \rho_s/\rho \gtrsim 1.2$, to ensure computational stability. The resulting coupling is referred to as TUCANMB. For more details, the reader is referred to Arranz et al. (2022b).

TUCAN and TUCANMB have both been extensively validated and successfully employed, as shown, among others, in Martínez-Muriel and Flores (2020) and Moriche et al. (2021) for the former and Arranz et al. (2022a), Martínez-Muriel et al. (2023) and Martínez-Muriel et al. (2024a) for the latter.

2.3. Computational set-up

Numerical simulations of the fluid interaction problem described in the previous section are performed in a computational domain with dimensions $19c \times 16c$ in the streamwise and vertical directions respectively. The domain is discretized by a uniform Cartesian grid with spacing $\Delta r = c/128$. The time step is selected such that the $CFL = U_{\max}\Delta t/\Delta r$ number is lower than 0.1. The size of the domain and the spatial and temporal resolution are defined based on the grid sensitivity analysis presented in Appendix B. The origin of the reference system is located at the leading edge of the airfoil. The free-stream inflow is modeled as a Dirichlet boundary condition at the inlet boundary ($x = -8c$), and the outflow has been modeled with an advective boundary condition ($\partial \boldsymbol{u}/\partial t + U_\infty \partial \boldsymbol{u}/\partial x = 0$) at the outlet ($x = 11c$). Free-slip boundary conditions are set at the lateral boundaries. A sketch of the computational set-up is shown in Fig. 2.

After four cycles, periodicity in both the forces and the flow in the vicinity of the airfoil is achieved in all the cases presented in this work.

3. Results

In this section, we characterize the performance of the passive flap described in Section 2 to reduce fluctuations of the aerodynamic loads under perturbations of the angle of attack. A total of 63 simulations were performed in this study, spanning the parametric space presented in Table 1. The database is available at Martínez-Muriel et al. (2024b).

3.1. Effect of flap-to-chord length ratio under different kinematics

To provide a general description of the database, four cases are selected for analysis (A1, A2, A3 and B3, as reported in Table 2). For each case, five different values of the flap to chord ratio are considered, namely $a/c = 0, 0.25, 0.375, 0.5$ and 0.75. The four selected cases have a non-zero geometric angle of attack, $\alpha = 5°$, and a density ratio $\rho^* = 1.5$.

Fig. 3 shows the time evolution of the lift coefficient, C_l, for the four cases and all flap lengths. The heaving motion of the airfoil leads to an unsteady, periodic aerodynamic response with positive C_l fluctuations during the downstroke ($0 \le t/T \le 0.5$) and negative C_l fluctuations during the upstroke ($0.5 \le t/T \le 1$). We can observe that for case A1, which has moderate values of $\kappa = 0.3$ and $h_0/c = 0.15$, upstroke and downstroke are relatively symmetric and C_l peaks at mid-stroke, when the effective angle of attack is maximum. This occurs even if the mean angle of attack is $\alpha = 5°$, which suggests that the aerodynamic response is roughly linear

Table 2
Parameters and mean lift coefficient of the cases selected for analysis in §3.1.

Case	α	κ	h_0/c	ρ^*	$\overline{C_l}$				
					$a/c = 0$	$a/c = 0.25$	$a/c = 0.375$	$a/c = 0.5$	$a/c = 0.75$
A1	5°	0.3	0.15	1.5	0.216	0.218	0.212	0.214	0.214
A2	5°	0.3	0.25	1.5	0.189	0.178	0.165	0.187	0.209
A3	5°	0.3	0.5	1.5	0.308	0.201	0.162	0.145	0.159
B3	5°	0.5	0.5	1.5	0.413	0.228	0.151	0.147	0.095

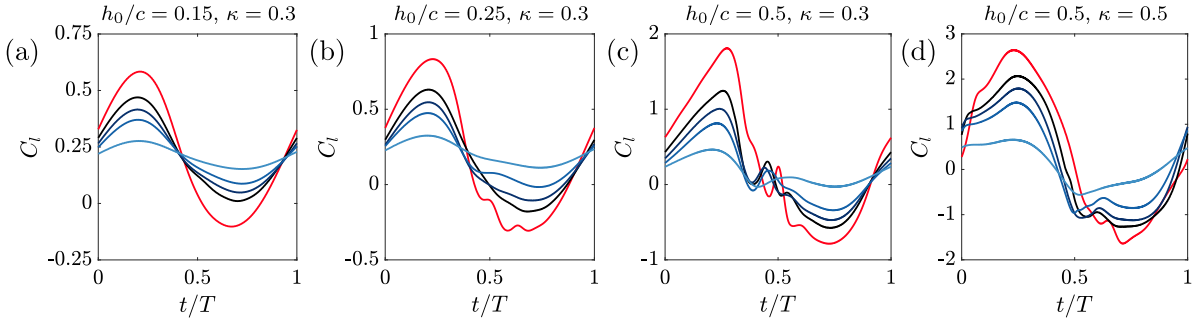

Fig. 3. Temporal evolution of the lift coefficient C_l for cases (a) A1, (b) A2, (c) A3, and (d) B3. Line colors correspond to different flap lengths: $a/c = 0$, $a/c = 0.25$, $a/c = 0.375$, $a/c = 0.5$, $a/c = 0.75$.

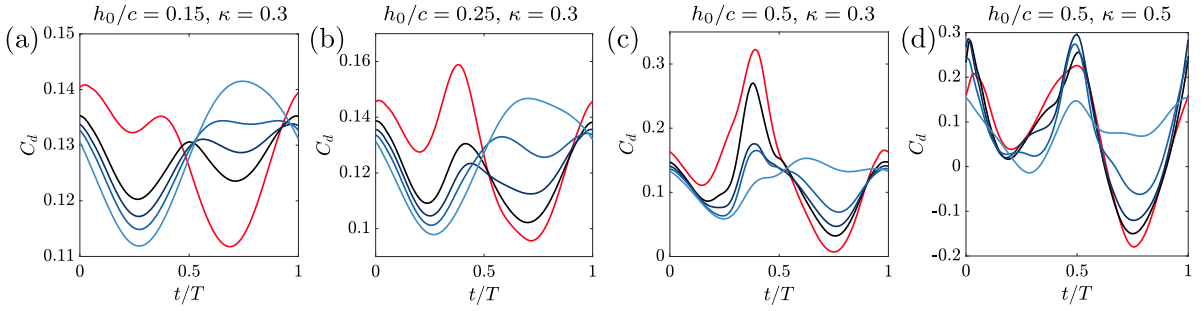

Fig. 4. Temporal evolution of the drag coefficient C_d for cases (a) A1, (b) A2, (c) A3, and (d) B3. Line colors correspond to different flap lengths: $a/c = 0$, $a/c = 0.25$, $a/c = 0.375$, $a/c = 0.5$, $a/c = 0.75$.

and the flap can be considered as a small perturbation. Indeed, Table 2 shows that the mean value of C_l is roughly independent on the flap to chord ratio for case A1.

As h_0/c increases (cases A2 and A3, Fig. 3b and c) the perturbation of C_l becomes stronger (note the difference in the y-axis scale of Figs. 3a, b and c) and the symmetry between upstroke and downstroke is broken. Also, the mean value of C_l becomes dependent on the flap to chord ratio, contrary to what was observed for case A1. The evolution of C_l with time for case A3 is reminiscent of the results observed for pitching foils (Otomo et al., 2021) and plunging airfoils with large leading-edge vortices (Moriche et al., 2021): a linear increase of C_l with time while the LEV develops and grows, followed by a sharp decrease in C_l when the LEV detaches and is advected downstream. Increasing κ (case B3, Fig. 3d) results in a more extreme aerodynamic response, with larger perturbations in C_l, a more irregular build-up of C_l during the downstroke and softer decrease in C_l at the end of the downstroke. Note that, besides the differences in the C_l evolution with the kinematics, the effect of the flap to chord length ratio is qualitatively similar in all cases in Fig. 3. As a/c increases, the perturbations in C_l become smaller, with considerable reductions obtained for $a/c = 0.75$. This effect will be properly quantified for the whole database in Section 3.2.

For completeness, Fig. 4 shows the time evolution of the drag coefficient C_d for cases A1, A2, A3 and B3. Overall, increasing the flap length results in lower drag during the downstroke ($0 < t/T < 0.5$) and higher drag during the upstroke ($0.5 < t/T < 1$). Sharp C_d maxima are observed whenever C_l varies abruptly (i.e., $t/T \approx 0.5$ for case A3, and $t/T \approx 0$ and 0.5 for case B3), suggesting a link between both phenomena. All cases generate net drag, as expected for a heaving airfoil at the low-Reynolds number considered here. Only case B3 is able to generate some thrust ($C_d < 0$), and it only occurs during the upstroke. Consistently with the previous observation, increasing the flap length reduces thrust generation (i.e., increases drag in the upstroke).

To better understand the effect of the flap on the evolution of C_l and C_d, Fig. 5 shows the evolution of the deflection angle of the flap, $\delta(t)$, for the same four cases depicted in Fig. 3.

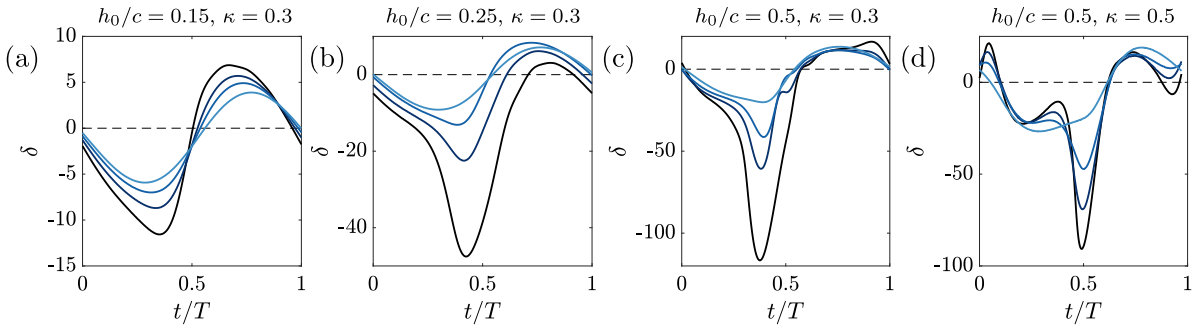

Fig. 5. Temporal evolution of the flap deflection angle δ for cases (a) A1, (b) A2, (c) A3, and (d) B3. Line colors correspond to different flap lengths: $a/c = 0.25$, $a/c = 0.375$, $a/c = 0.5$, $a/c = 0.75$.

Case A1 in Fig. 5a shows small-amplitude quasi-symmetric flap deflections, particularly for $a/c = 0.375, 0.5$ and 0.75. During the downstroke ($0 \leq t/T \leq 0.5$) the pressure difference between the upper and lower surface of the flap produces a negative torque on the hinge, yielding a negative deflection of the flap (i.e., counterclockwise). The negative deflection of the flap induces a negative camber in the airfoil and a reduction of the effective angle of attack of the airfoil, which reduces the instantaneous C_l. This can be observed in Fig. 3a, where the flapped airfoils show smaller positive fluctuation of the instantaneous C_l than the rigid airfoil during the downstroke. During the upstroke ($0.5 \leq t/T \leq 1.0$) the pressure difference in the flap changes sign, resulting in positive values of δ and a larger instantaneous C_l for the flapped airfoils.

It is worth noting that, besides the small-amplitude flap deflections observed in case A1, the results shown in Fig. 5a differ considerably from the linear QS model proposed by Arredondo-Galeana et al. (2021). Specifically, the QS model predicts maximum flap deflections that increase in amplitude with a/c (see Eq. (7) in Appendix A), but the simulation data shows the opposite trend. This suggests that unsteady effects due to inertia and/or aerodynamics are important, even for the relatively slow and low-amplitude kinematics of case A1.

The flap deflections of cases A2 and A3 in Fig. 5b and c are qualitatively similar to the results for case A1, except for the development of an extreme (negative) deflection of the flap during the second half of the downstroke. These extreme flap deflections are more apparent for small flaps, and are consistent with the development of more abrupt changes in C_l and sharper C_d maxima as h_0/c increases, as discussed in Figs. 3 and 4. For more extreme kinematics (case B3, Fig. 5d) the peak of δ is somewhat delayed, coincident with the end of the abrupt decrease of C_l (see Fig. 3d) and a sharp maxima in C_d (see Fig. 4d). Overall, the amplitude of the fluctuations of δ decrease as the flap to chord ratio increases, consistent with an increase of the flap inertia.

The temporal evolutions of the lift coefficient and the flap deflections shown in Figs. 3 and 5 suggest a transition from the quasi-symmetric linear response observed in case A1 to the non-linear responses of cases A2, A3 and B3. In order to characterize the physical phenomena behind this transition, Figs. 6–8 show instantaneous visualizations of the flow around the airfoils.

The colored contours show the vorticity, which allows simple visualization of the boundary layers over the airfoil and of the formation of vortical structures (both over the airfoil, and in the airfoil's wake). To facilitate the identification of these vortices, Fig. 6–8 also include a contour of $\lambda_2 = -5U_\infty^2/c^2$, following the vortex identification method of Jeong and Hussain (1995). Note that Figs. 6–8 only show a few representative snapshots of the selected cases. The interested reader can find the videos for all flap lengths of cases A1, A2, A3 and B3 in the supplementary material available in the Zenodo repository (Martínez-Muriel et al., 2024b).

The instantaneous visualizations of case A1 (Fig. 6) shows relatively thin boundary layers on the pressure side (lower surface) of the airfoil, that remain attached at all times. On the suction side (upper surface) the boundary layer that develops from the stagnation point at the leading edge of the airfoil grows due to the adverse pressure gradient (not shown), and, at mid-downstroke, it separates around $x/c = 1/4$ for the $a/c = 0.25$ case, and around $x/c = 3/4$ for the $a/c = 0.75$ case, as indicated by the black dots on Fig. 6. The separation of the boundary layer is determined by selecting the first x/c location with $\omega = 0$ on the suction surface, meaning zero wall shear stress. The deflection of the flap seems to be able to partially reattach the separated boundary layer more effectively for the long flap ($a/c = 0.75$, right column in Fig. 6) than for the short flap ($a/c = 0.25$, left column of Fig. 6), probably because the deflection of the longer flap has a stronger effect on the camber along a large portion of the airfoil that smooths the pressure gradient on the upper surface.

Contrary to the quasi-steady, quasi-linear evolution of case A1, case B3 develops unsteady non-linear vortical dynamics. The stronger production of vorticity near the leading edge results in the roll-up of the separated boundary layers, generating coherent LEVs in the suction and pressure sides of the airfoil. Fig. 7 depicts the evolution of the suction side LEV (in red), but the interested reader can examine the evolution of the pressure side LEV (in blue) in the videos provided with the supplementary material (Martínez-Muriel et al., 2024b). During the downstroke, Fig. 7 shows how the suction side LEV separates from the airfoil and travels downstream. When it advects over the flap, the low-pressure region associated to the LEV produces a strong counterclockwise torque on the flap, which triggers the extreme flap deflections observed in Fig. 5d at $t/T = 0.5$. Indeed, this time corresponds to the arrival of the LEV to the TE of the airfoil (Fig. 7e-f), when the torque produced on the flap by the low-pressure region of the LEV is maximum. Of note, the videos of case B3 in the supplementary material (Martínez-Muriel et al., 2024b) show a similar interaction

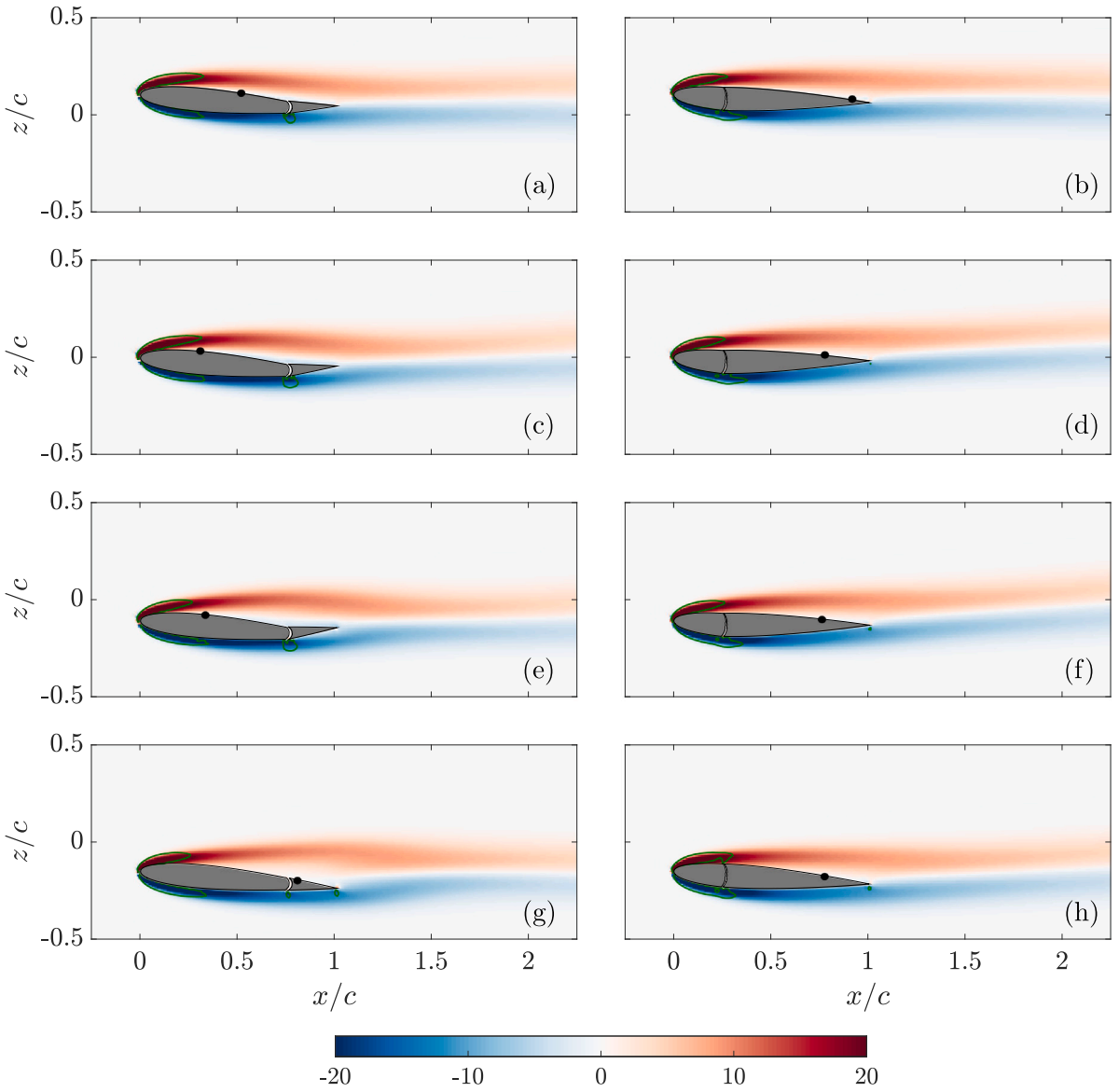

Fig. 6. Vorticity, $\omega c/U_\infty$, contours for case A1 ($h_0/c = 0.15, \kappa = 0.3$). Left column, $a/c = 0.25$. Right column, $a/c = 0.75$. Time instants correspond to (a, b) $t/T = 0.125$, (c, d) $t/T = 0.25$, (e, f) $t/T = 0.375$, (g, h) $t/T = 0.5$. The green line corresponds to $\lambda_2 = -5U_\infty^2/c^2$. The black dots corresponds to $\omega = 0$ on the suction (upper) side of the airfoil, and represent the separation point of the boundary layer.

between the weaker LEV developed on the pressure side and the flap, which explains the weaker positive peak in $\delta(t)$ at $t/T \approx 0.1$ observed in Fig. 5d.

When the flap is sufficiently large, the LEV dynamics depicted in Fig. 7 is disrupted. This is shown in Fig. 8, which presents the vorticity distribution for different flap lengths, including $a/c = 0$, at mid-downstroke, $t/T = 0.25$.

The shape, position and intensity of the LEV for cases with $a/c = 0, 0.25$ and 0.5 are virtually identical. But the shape and position of the LEV of the case with the largest flap ($a/c = 0.75$, Fig. 8d) is different from the rest. This is not surprising, since for the latter, the LEV is already well over the flap for $t/T = 0.25$. The difference in the shape and position of the LEV in case B3 with $a/c = 0.75$ explains the complete absence of a negative peak in the flap deflection for this configuration, as shown by the light blue curve in Fig. 5d.

The instantaneous visualizations of cases A2 and A3 correspond to situations intermediate between A1 and B3, as shown in Fig. 9. Case A2 is characterized by larger separated regions than in A1 (compare Fig. 9a and b), that do not trigger the formation of LEVs. As shown in the videos in the supplementary material, the large deflection of the flap in case A2 results in the formation of a counter-rotating dipole in the wake of the airfoil: in the suction side, the interaction of the trailing edge of the flap with the

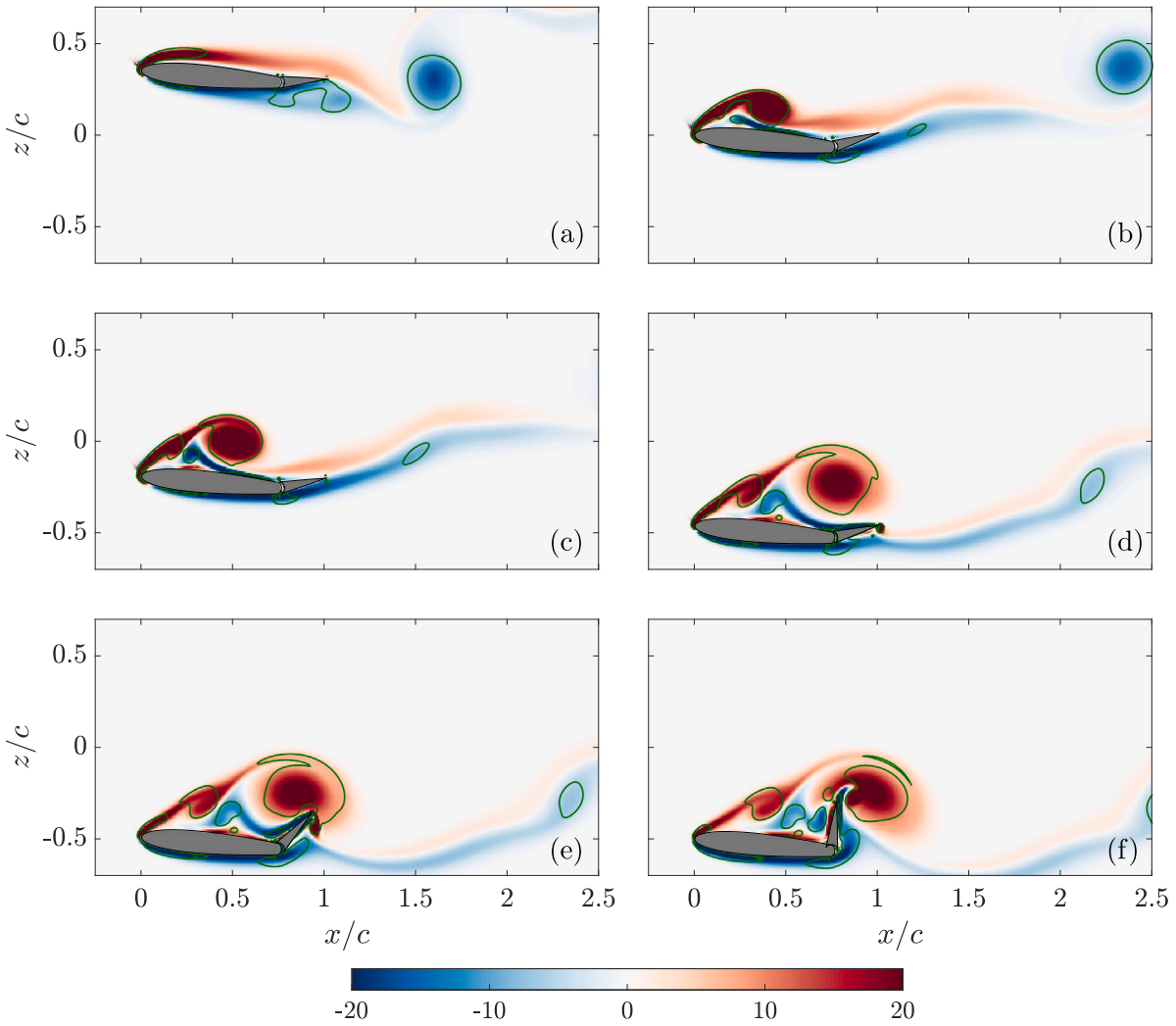

Fig. 7. Vorticity, $\omega c/U_\infty$, contours for case B3 ($h_0/c = 0.5, \kappa = 0.5$), $a/c = 0.25$. Time instants correspond to (a) $t/T = 0.125$, (b) $t/T = 0.25$, (c) $t/T \approx 0.31$, (d) $t/T \approx 0.43$, (e) $t/T \approx 0.46$, (f) $t/T = 0.5$. The green line corresponds to $\lambda_2 = -5U_\infty^2/c^2$.

separated shear layer yields a clockwise vortex in the wake, while in the pressure side the separation of the boundary layer at the hinge of the flap produces a counterclockwise vortex. Case A3 shows a LEV that forms at about $x/c = 0.75$, further downstream than in case B3 (compare Figs. 9c and d). This LEV moves closer to the upper surface than the LEV in B3, which results in a stronger interaction with the flap, and the formation of a counter rotating trailing edge vortex at the lower surface, as shown in the videos in the supplementary material.

Finally, symmetric cases with $\alpha = 0°$ (not shown) exhibit similar separated boundary layers and LEVs as those discussed for cases A1, A2, A3 and B3, except for the symmetry observed between the upstroke and downstroke in the velocity fields, force coefficients, and flap deflections.

3.2. Load mitigation

Two main observations can be made after having analyzed the cases described in Table 2. First, the amplitude of the temporal evolution of the lift coefficient, $C_l(t)$, decreases with increasing a/c (i.e., with larger flap size), supporting the effectiveness of such a device for unsteady load mitigation. However, a quantitative measure of the unsteady load mitigation is still required. Second, for cases with $\alpha = 5°$, the fluctuation of $C_l(t)$ is not symmetric during downstroke and upstroke, and the mean value of $C_l(t)$ differs from that of the rigid case ($a/c = 0$). In fact, both $\overline{C_l}$ and $\overline{C_d}$ depend on a/c and the airfoil kinematics ($\kappa, h_0/c$), as shown in Fig. 10. The mean lift coefficient of all cases with $\alpha = 5°$ and $\rho^* = 1.5$ is provided in Fig. 10a. At the lowest heaving amplitudes ($h_0/c = 0.15$), all cases report very similar values of $\overline{C_l}$, regardless of the reduced frequency. However, in the case with $h_0/c = 0.25$ and $k = 0.5$, and in all cases with $h_0/c = 0.5$, the values obtained for flapped foils clearly deviate from those for rigid foils. Larger differences are

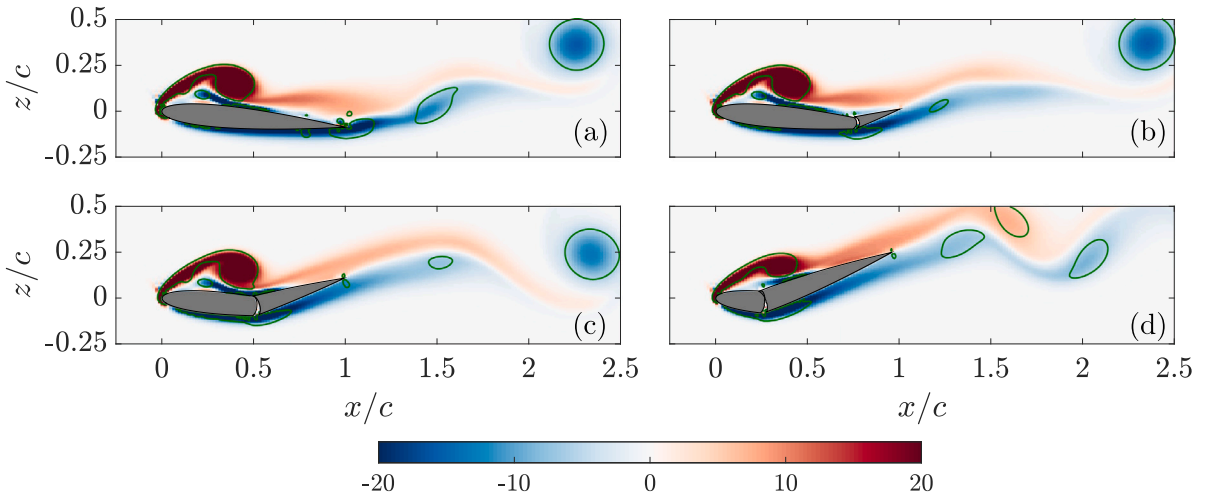

Fig. 8. Vorticity, $\omega c/U_\infty$, contours at $t/T = 0.25$ for case B3 ($h_0/c = 0.5, \kappa = 0.5$) with flap-to-chord length ratios (a) $a/c = 0$, (b) $a/c = 0.25$, (c) $a/c = 0.5$, (d) $a/c = 0.75$. The green line corresponds to $\lambda_2 = -5U_\infty^2/c^2$.

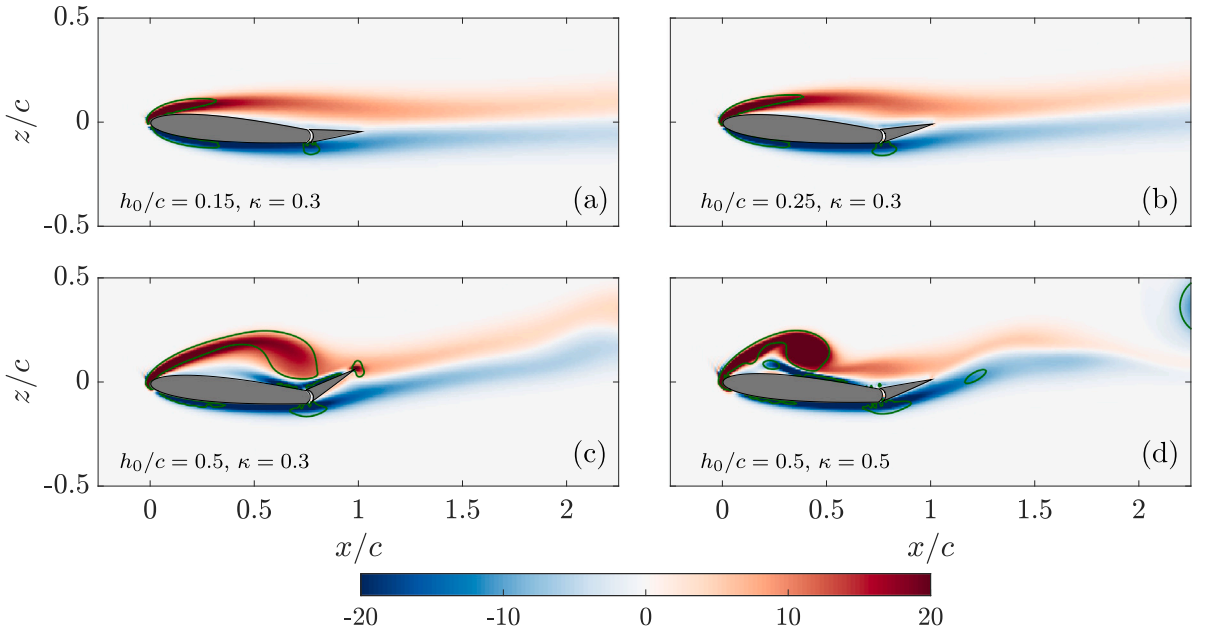

Fig. 9. Vorticity, $\omega c/U_\infty$, contours for cases (a) A1, (b) A2, (c) A3 and (d) B3. All cases are shown at $t/T = 0.25$. The green line corresponds to $\lambda_2 = -5U_\infty^2/c^2$.

observed as the kinematic become more intense (i.e., larger amplitude, higher reduced frequency), likely due to the development of a stronger LEV. The mean drag coefficient $\overline{C_d}$ for all simulated cases with $\rho^* = 1.5$ is shown in Fig. 10b, showing increasing variability as the heaving amplitude increases. Notably, cases with $\kappa = 0.5$ report a smaller value of $\overline{C_d}$ compared to those with $\kappa = 0.3$. This effect is particularly pronounced at the largest amplitude, $h_0/c = 0.5$, and it is caused by the suction peaks associated to the LEVs. For instance, case B3 shows instantaneous thrust generation during the upstroke ($0.5 < t/T < 1$, see Fig. 4d), which is caused by the strong LEV developing in the lower surface (see videos in the Supplementary Material) and the positive geometric angle of attack of the airfoil (which favors the projection of the suction force associated to the LEV core along the negative x direction). Increasing the length of the flap in case B3 disrupts the LEV development (i.e., note the blue vortex around $x/c = 2.25$ in Fig. 8), increasing the drag during the upstroke and consequently increasing $\overline{C_d}$.

Next, we quantify the load mitigation for each of the cases. We define the load mitigation factor as

$$R_F = 1 - \frac{\mathrm{STD}\left(C_l^F\right)}{\mathrm{STD}\left(C_l^R\right)}, \tag{4}$$

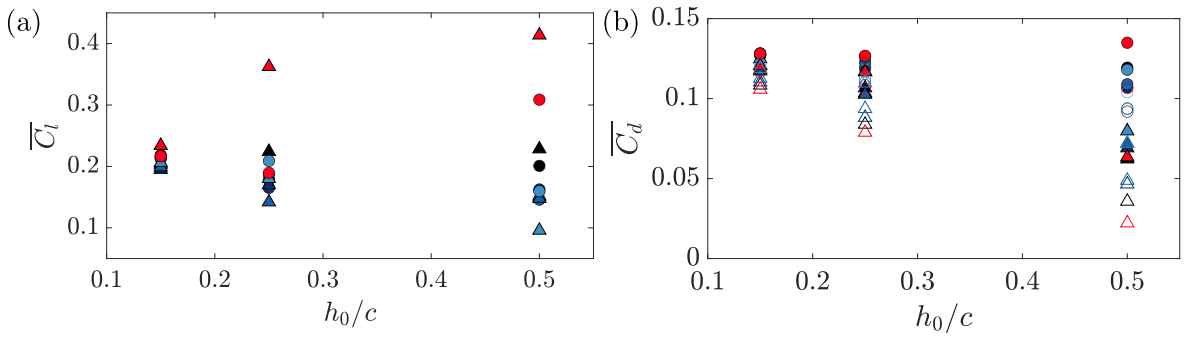

Fig. 10. (a) Mean lift coefficient $\overline{C_l}$ for $\alpha = 5°$ cases. (b) Mean drag coefficient $\overline{C_d}$ for $\alpha = 0°$ (empty) and $\alpha = 5°$ (filled) cases. Circles and triangles correspond to $\kappa = 0.3$ and $\kappa = 0.5$, respectively. Colors correspond to ——: $a/c = 0$, ——: $a/c = 0.25$, ——: $a/c = 0.375$, ——: $a/c = 0.5$, ——: $a/c = 0.75$.

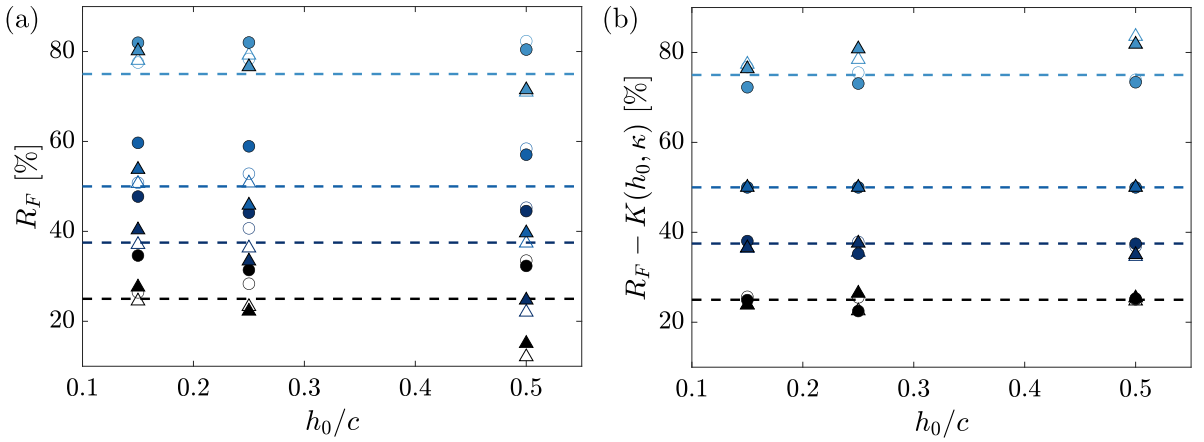

Fig. 11. (a) Reduction in fluctuations R_F and (b) corrected reduction in fluctuations $R_F - K(h_0, \kappa)$ for all cases. Circles and triangles correspond to $\kappa = 0.3$ and $\kappa = 0.5$, respectively. Colors correspond to ——: $a/c = 0.25$, ——: $a/c = 0.375$, ——: $a/c = 0.5$, ——: $a/c = 0.75$. Empty and filled markers correspond to $\alpha = 0°$ and $\alpha = 5°$, respectively.

where C_l is the time-dependent lift coefficient, the standard deviation (STD) is computed over time, and the superscripts F, R refer to flapped and rigid cases, respectively. Note that this definition of R_F is equivalent to that used by Arredondo-Galeana et al. (2021), except for the fact that they estimated STD(C_l) using only the first mode of the Fourier decomposition of $C_l(t)$.

The load mitigation factors of the present simulations are shown in Fig. 11a. The horizontal dashed lines corresponds to the prediction from the Quasi-Steady (QS) of Arredondo-Galeana et al. (2021), described in Appendix A. Overall, the simulations results show good qualitative agreement with the predictions of the QS model (i.e., $R_{QS} \approx a/c$, represented as horizontal dashed lines in Fig. 11). The deviations with respect to the QS prediction seems to become stronger for the more energetic kinematics, in agreement with the experimental validation of Arredondo-Galeana et al. (2021), who suggested that the cause of the deviation might lie in the flow separation over the airfoils, a condition that violates the attached flow hypothesis of the QS model.

Flow separation is a dominant phenomenon in our database (see Figs. 6–9), run at Reynolds number $Re = 1000$ (for reference, the experiments in Arredondo-Galeana et al. (2021) had $Re = 50000$). The effect of flow separation is apparent also on the values of the mean lift coefficient (Fig. 10), which are roughly half than those reported by Arredondo-Galeana et al. (2021). It is interesting to note that, in many cases, flow separation is not detrimental for the load mitigation factor. Most data points in Fig. 11 lie above their corresponding dashed line, indicating a greater reduction in the lift fluctuations than predicted by the QS model. The cases yielding values of R_F lower than the QS prediction are generally those with the most extreme kinematics, in agreement with the findings of Arredondo-Galeana et al. (2021). In the present database, the maximum discrepancy between the results presented in Fig. 11a and the QS model is found for the case with $a/c = 0.375$, $\alpha = 0$, $\kappa = 0.5$, $h_0/c = 0.5$. The load mitigation predicted by the QS model for this case was $R_{QS} = 0.375$, but the value obtained in the simulations was $R_F = 0.22$. As expected, this case exhibits massive boundary later separation and strong LEVs developing during both upstroke and downstroke, as shown in the Supplementary Material videos (Martínez-Muriel et al., 2024b).

The analysis of the data in Fig. 11*a* shows that the deviations in R_F with respect to R_{QS} depend on both κ and h_0/c. Indeed, the scatter shown in Fig. 11*a* is similar to the scatter observed when R_F is plotted as a function of α_0' (not shown). Of note, it can be observed in Fig. 11*a* that a variation in the flap-to-chord length ratio, $\Delta a/c$, leads to a roughly equal variation in the reduction

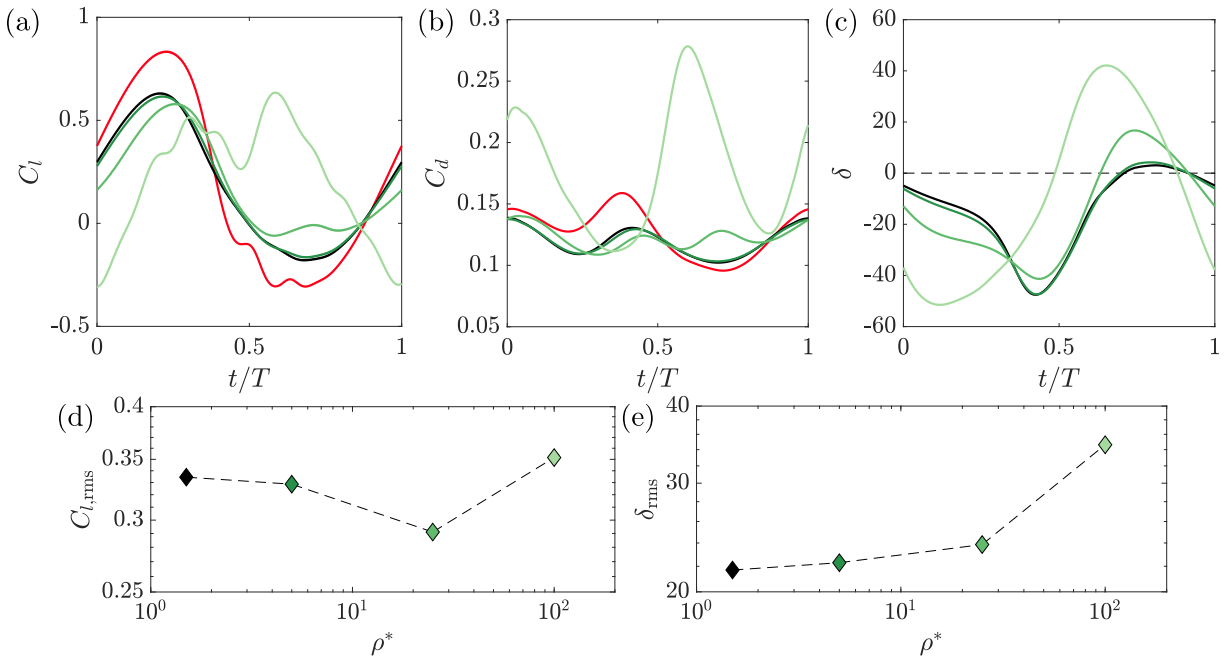

Fig. 12. Temporal evolution of (a) lift coefficient C_l, (b) drag coefficient C_d and (c) flap deflection δ of cases with $\kappa = 0.3$, $h_0/c = 0.25$. In red, ——: $a/c = 0$, in greens: $a/c = 0.25$, where ——: $\rho^* = 1.5$, ——: $\rho^* = 5$, ——: $\rho^* = 25$, ——: $\rho^* = 100$. Evolution of (d) RMS of the lift coefficient, $C_{l,\mathrm{rms}}$ and (e) RMS of the flap deflection, δ_{rms}, with the density ratio, ρ^*.

of fluctuations, ΔR_F. This observation allows proposing a modification of Eq. (4) introducing a term $K(h_0, \kappa)$ that depends only on kinematics and not on a/c, to account for the difference between expected and actual values. To determine K, only a simulation with an intermediate value of a/c should be needed to predict the value of R_F for any a/c. Results for the corrected reduction in fluctuations are shown in Fig. 11b. The reduction in fluctuations have been adjusted so that the error for cases with $a/c = 0.5$ is zero. The selection of the value of $a/c = 0.5$ was arbitrary. Clearly, the discrepancies between the computed load mitigation factor and the value predicted by the QS model have been reduced. Thus, $R_{QS} + K(h_0, \kappa)$ can be used to predict the load mitigation factor for all cases with same h_0, κ but different a/c. Still, some deviations remain, especially for cases with $\kappa = 0.5, a/c = 0.75$, indicating that more advanced tools may be needed in the future to predict the exact load mitigation.

3.3. Effect of inertia

We analyze now the effect of the inertia of the flap on its dynamics and the aerodynamic response of the airfoil by modifying the density ratio. Consider now cases with the same kinematics as A2 ($\kappa = 0.3$, $h_0/c = 0.25$) and $a/c = 0.25$, with flaps characterized by density ratios equal to $\rho^* = 1.5, 5, 25$ and 100. The temporal evolution of C_l, C_d, and δ for these cases is shown in Fig. 12(a,b,c). The $a/c = 0$ case is also included in red. There are no significant changes in any of the measured quantities when comparing the flaps with $\rho^* = 1.5$ with $\rho^* = 5$. When looking at the case with $\rho^* = 25$, the evolution of the lift coefficient is delayed during the first instants of the period with respect to $\rho^* \leq 5$ cases. Moreover, a larger value of $\overline{C_l}$ is obtained when compared to $\rho^* \leq 5$ due to an increase in C_l within the interval $t/T \approx 0.6 - 0.8$. This is mainly due to the positive flap deflections that are found at the same time interval. In fact, despite that the maximum of the absolute value of the flap deflection $|\delta|_{\max}$ is reduced, the fluctuations of the flap deflection are increased. When the value of the density ratio is increased to $\rho^* = 100$, the temporal evolution of all variables changes substantially. The lift coefficient presents two positive peaks compared to the only one seen for the rest of the cases. The two peaks are the product of a positive balance between the oscillations in the angle of attack due to heaving and the instantaneous shape of the airfoil that changes with the flap deflection. In fact, the second peak in mainly caused by the large positive deflection of the flap during the first part of the upstroke. The mean drag coefficient is a 65% larger than the one yielded by the rigid case.

Figs. 12(d,e) show the RMS values of the lift coefficient, $C_{l,\mathrm{rms}}$ and the flap deflections, δ_{rms}, respectively. While the value of the RMS of the lift coefficient is reduced when increasing the density ratio up to $\rho^* = 25$, it peaks up when the density ratio is further increased to $\rho^* = 100$. This non-monotonic evolution of $C_{l,\mathrm{rms}}$ with the density ratio contrasts with the monotonic evolution of δ_{rms}. This highlights the importance of selecting the flap's inertia for its impact on response and dynamics. On the other hand, as the effect of ρ^* on the dynamics of the flap and the temporal evolution of the forces is negligible when the density ratio is in the range of $\rho^* \sim \mathcal{O}(1)$, the discrepancies with the QS model cannot be explained in terms of inertia.

4. Conclusions

The unsteady load fluctuations that can be mitigated using a passive-pitching trailing-edge flap on airfoils subjected to oscillations in the angle of attack at $Re = 1000$ have been examined by performing direct numerical simulations of the fluid–structure interaction problem. A range of flap-to-chord length ratios a/c were tested at different kinematics, while varying other quantities in the parametric space as the solid-to-fluid density ratio ρ^*.

The results show significant variability in the temporal evolution of the lift coefficient, drag coefficient and flap deflections with a/c and with the amplitude of the oscillations in the angle of attack given by the different kinematics. For moderate values of the oscillation amplitude, both aerodynamic force coefficients (lift and drag) and the flap deflection present smooth temporal evolutions. However, the cases with the most intense kinematics, characterized by larger angle of attack oscillations, exhibit sharper temporal evolutions for the aerodynamic force coefficients and flap deflections. Instantaneous visualizations of these cases show significant boundary layer separation and the formation of strong Leading Edge Vortices (LEV). The interactions of the separated boundary layers and the LEVs with the passive flap modify the flow dynamics, resulting in a consistent reduction in the mean drag and in the fluctuations of lift and drag coefficients as the flap size (a/c) increases.

Indeed, the load mitigation that is obtained for the majority of the cases is close to be proportional to a/c, highlighting the potential of larger flaps to enhance load mitigation under the considered conditions. This behavior aligns with predictions of the quasi-steady model proposed by Arredondo-Galeana et al. (2021), which assumes attached flow conditions and does not consider aerodynamic non-linearities or inertia effects. Interestingly, many of the cases report a mitigation larger than the expected one. However, a notable departure was observed between the predictions of the quasi-steady model and the actual flap deflections for the cases with the most intense kinematics, with a load mitigation lower than predicted. This is consistent with the measurements of Arredondo-Galeana et al. (2021) performed at a 50 times greater Reynolds number, and shows the need for refined models to accurately predict the load mitigation in complex scenarios.

Finally, the study further explores the effect of the inertia on the dynamics of the airfoil through a change in the density ratio. The load mitigation presents a non-linear trend with increasing inertia, emphasizing the relevance of the proper selection of the parameters to achieve optimal performance and to develop energy-efficient control strategies tailored to operate in unsteady flow conditions.

CRediT authorship contribution statement

C. Martínez-Muriel: Writing – review & editing, Writing – original draft, Visualization, Software, Methodology, Investigation, Formal analysis. **I.M. Viola:** Writing – review & editing, Supervision, Conceptualization. **M. García-Villalba:** Writing – review & editing, Supervision, Funding acquisition, Conceptualization. **O. Flores:** Writing – review & editing, Writing – original draft, Supervision, Project administration, Funding acquisition, Conceptualization.

Declaration of competing interest

The authors declare the following financial interests/personal relationships which may be considered as potential competing interests: Oscar Flores reports financial support was provided by Agencia Estatal de Investigación, España. If there are other authors, they declare that they have no known competing financial interests or personal relationships that could have appeared to influence the work reported in this paper.

Acknowledgments

This work was partially supported by grant DPI2016-76151-C2-2-R (AEI/FEDER, UE). The supplementary material can be found in the Zenodo repository: Martínez-Muriel et al. (2024b).

Appendix A. Theoretical model

The model for load mitigation proposed by Arredondo-Galeana et al. (2021) is based on the same unsteady potential theory for thin airfoils as the pioneering work of Theodorsen (1935) and Garrick (1936). Let us consider a rigid symmetric airfoil free to rotate (an angle θ') around its leading edge. It would align with the incoming flow after a change in its direction, leading to zero lift force. In order to generate lift force on the airfoil, there must be a moment M_s that opposes the hydrodynamic pitching moment M_h acting on the pitching axis of the airfoil, such that the airfoil is set to a given angle of attack α. This moment M_s can be provided by a highly flexible torsional spring, which, if highly preloaded (i.e. $\theta_p \gg \theta'$), has a virtually constant moment

$$M_s = k_s(\theta_p \pm \theta') \approx k_s\theta_p \tag{5}$$

that would ensure $M_s = -M_h$. Consider now the instantaneous change in the angle of attack α'. Using linear thin airfoil theory, this increment in the angle of attack results in an increment in lift $\Delta L_1 = 2\pi\alpha'$ and an increment in the hydrodynamic pitching moment $\Delta M_h = -\Delta L_1 x_{AC}$, where x_{AC} is the position of the aerodynamic center measured from the leading edge. This increase in moment

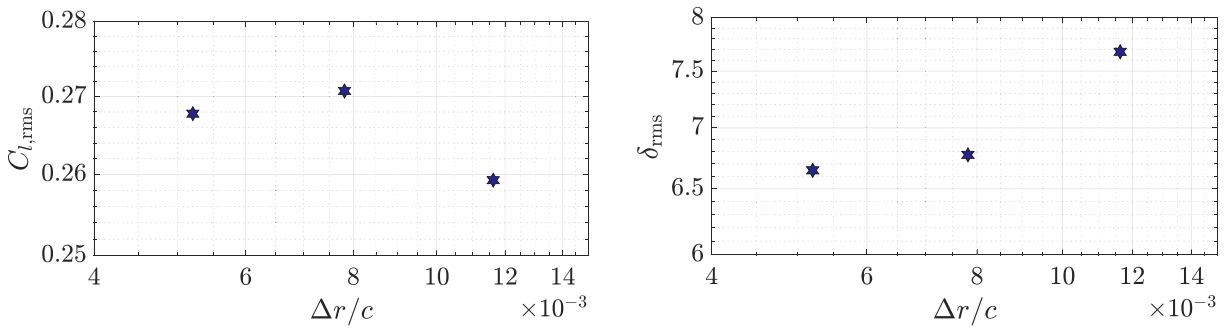

Fig. 13. Evolution of (*a*) RMS of lift coefficient, $C_{l,\mathrm{rms}}$, and (*b*) RMS of flap deflection δ_{rms} with the grid spacing $\Delta r/c$ for case A1 in Table 2.

will lead to a counterclockwise re-pitch of the airfoil by an angle $\theta' < 0$, which leads to an additional change in lift $\Delta L_2 = 2\pi\theta'$, modifying ΔM_h. As stated in Eq. (5), the moment delivered by the spring is constant, such that

$$M_s = -(M_h + \Delta M_h), \tag{6}$$

which leads to $\Delta M_h = 0$, implying that $\alpha' = -\theta'$, and the load of the airfoil remains unchanged.

Now, to predict the load that can be mitigated on a rigid airfoil when is subjected to oscillations in the angle of attack, a linear, quasi-steady (QS) panel method, based on the potential flow hypotheses is used. The load is intended to be mitigated attaching a passive-pitching trailing-edge (TE) flap to the foil, hinged at a position x_p measured from the leading edge. In the panel method, the rigid foil and the TE flap are considered to be two separate panels, which are characterized by a circulation γ_1 and γ_2 respectively. After an increment in the angle of attack α', the circulation of the first panel becomes $\gamma_1 + \Delta\gamma_1$, while the circulation of the second panel remains γ_2 after a counterclockwise deflection δ_{QS} of the flap. After some algebra, it is found that the flap deflection only depends on the increment in the angle of attack and the position of the hinge following the expression

$$\delta_{QS} = -\alpha' \left(1 - \frac{2x_p}{3c}\right). \tag{7}$$

The instantaneous lift coefficient is equal to

$$\Delta C_l^F = 2\pi\alpha' \frac{x_p}{c}, \tag{8}$$

where the superscript F refers to the flexible (or flapped) cases. Normalizing Eq. (8) by the load increment in the rigid airfoil, i.e. $\Delta C_l^R = 2\pi\alpha'$, it is possible to find the load relative to the rigid case,

$$\Delta C_l^* = x_p/c, \tag{9}$$

which leads to the instantaneous load reduction

$$R_{QS} = 1 - \Delta C_l^* = 1 - x_p/c = a/c. \tag{10}$$

Given Eq. (10), the model predicts a linear relationship between the load reduction and the flap-to-chord length ratio. Of note, this result is consistent with Theodorsen's theory in the limit of vanishing reduced frequency. For more details about the load mitigation strategy proposed here, the reader is referred to Arredondo-Galeana et al. (2021).

Appendix B. Grid and domain sensitivity analysis

A grid sensitivity study is performed to select the spatial and temporal resolution to be employed in the simulations. The case A1 in Table 2 with $a/c = 0.25$ is selected as the benchmark case. Three different spatial resolutions Δr are considered, $c/86$, $c/128$, $c/156$, and will be specified using superscripts R, S and T, respectively. The bodies are discretized using the same Eulerian resolution. The temporal resolution is such that the $CFL = U_{\max}\Delta t/\Delta r$ number is always below 0.1. The grid sensitivity on the root-mean-square of the lift coefficient C_l and flap deflection δ, namely $C_{l,\mathrm{rms}}$ and, δ_{rms} is shown in Fig. 13.

The relative changes in $C_{l,\mathrm{rms}}$ when going from $c/86$ to $c/128$ are about 4%. When going from $c/128$ to $c/196$, relative changes become smaller than a 1%. Similar relative changes are obtained for δ_{rms}. The extrapolated value of δ_{rms} for an infinitely fine grid is achieved using Richardson extrapolation, that is,

$$\delta_{\mathrm{rms}}^{RE} = \delta_{\mathrm{rms}}^{\mathrm{T}} - \frac{\delta_{\mathrm{rms}}^{\mathrm{S}} - \delta_{\mathrm{rms}}^{\mathrm{T}}}{r^p - 1} = 6.62°, \quad \text{with } p = \log\left(\frac{\delta_{\mathrm{rms}}^{\mathrm{R}} - \delta_{\mathrm{rms}}^{\mathrm{S}}}{\delta_{\mathrm{rms}}^{\mathrm{S}} - \delta_{\mathrm{rms}}^{\mathrm{T}}}\right) / \log(r), \tag{11}$$

where $r = \Delta r^R/\Delta r^S = 1.5$. The relative errors on δ_{rms} with respect to the extrapolated value is, for the ith grid resolution,

$$\epsilon_\delta^i = \frac{|\delta_{\mathrm{rms}}^i - \delta_{\mathrm{rms}}^{RE}|}{\delta_{\mathrm{rms}}^{RE}} = 0.15, 0.02, \text{and } 0.003 \text{ for } i = 1, 2, \text{and } 3 \tag{12}$$

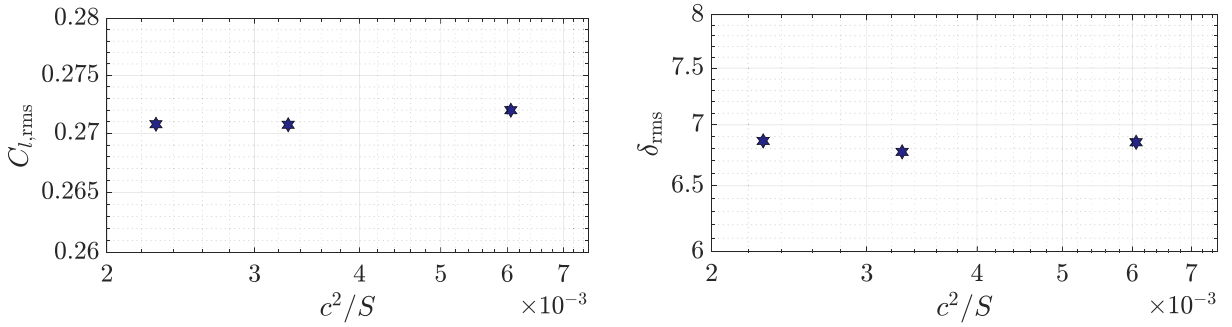

Fig. 14. Evolution of (*a*) RMS of lift coefficient, $C_{l,\mathrm{rms}}$, and (*b*) RMS of flap deflection δ_{rms} with the domain size c^2/S for case A1 in Table 2.

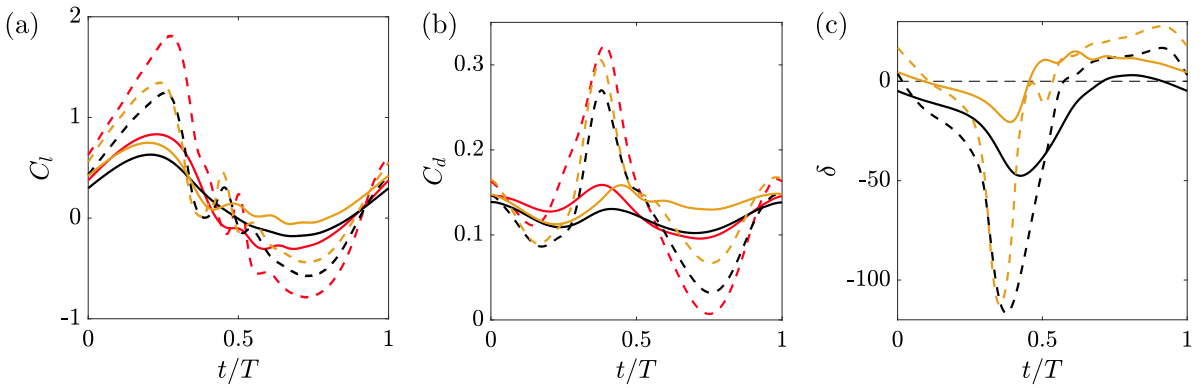

Fig. 15. Effect of the constant moment of the hinge on the temporal evolution of (*a*) lift coefficient C_l, (*b*) drag coefficient C_d and (*c*) flap deflection δ of cases with $\kappa = 0.3$. Line colors correspond to ——: $a/c = 0$, ——: $(a/c = 0.25, \delta_s)$, ——: $(a/c = 0.25, \delta_0)$. Line types correspond to ——: $h_0/c = 0.25$, — — —: $h_0/c = 0.5$.

Based on the obtained results, the simulations are performed with a spatial resolution $\Delta r = c/128$. The numerical uncertainty in the flap deflection, computed as in Viola et al. (2013), is $U_\delta = 0.1833°$.

Besides, the effect of the domain size on the same quantities is also characterized. Three different sizes are considered here: $(15c \times 12c)$, $(19c \times 16c)$, $(23c \times 20c)$. The results obtained for each of the domain sizes are shown in Fig. 14. It is possible to see that the effect of the domain size is almost negligible. As the analysis of the effect of resolution has been performed with a domain size $(19c \times 16c)$, the simulations are also performed using this domain.

Appendix C. Effect of constant moment

Regarding applicability, a reduction in the mean lift coefficient may lead to deviations from the design requirements of the device, even if fluctuations are effectively mitigated. To address this issue, the impact of applying a constant moment at the hinge and hence modifying the flap the flections is examined.

In particular, consider cases A2 and A3 with $a/c = 0.25$, which exhibit asymmetric flap deflections ($\bar{\delta} \neq 0$). Despite that, the mean lift coefficient $\overline{C_l}$ in case A2 closely matches that of the rigid foil. In contrast, the mean lift coefficient of the case A3 is $\overline{C_l} \approx 0.2$, differing from the rigid foil's value of $\overline{C_l} \approx 0.31$.

To achieve approximately symmetric flap deflections ($\bar{\delta} = 0$) over a cycle, the moment applied at the hinge for these two cases is now modified. These modified cases are denoted as δ_0, while those cases shown in Section 3.1, where the moment applied at the hinge was computed to have $\delta = 0$ at steady conditions, are denoted as δ_s. The temporal evolution of C_l, C_d and δ of cases A2 and A3 with $a/c = 0.25$, comparing both δ_d and δ_0 alternatives, alongside the rigid foil cases for reference, are shown in Fig. 15.

Following this adjustment in hinge moment, the δ_0 subcases exhibit upward shifts in all three variables with respect to the δ_s subcases. The effect of the change in the hinge moment is negligible on the reduction in load fluctuations, as both δ_0 and δ_s subcases achieve the same value of R_F. In case A3, this adjustment results in a mean lift coefficient comparable to the rigid foil. However, case A2 also shows an increased mean lift coefficient, reaching $\overline{C_l} = 0.275$, versus the $\overline{C_l} \approx 0.19$ for the rigid foil. Thus, the analysis shows the impossibility to achieve $\overline{C_l^F} = \overline{C_l^R}$ consistently across all kinematics in this study using a single value of the moment applied at the hinge. If maintaining this condition is essential, alternative solutions would need to be explored.

Data availability

Data will be made available on request.

References

Addo-Akoto, R., Han, J.S., Han, J.H., 2021. Roles of wing flexibility and kinematics in flapping wing aerodynamics. J. Fluids Struct. 104, 103317.

Alaminos-Quesada, J., 2021. Limit of the two-dimensional linear potential theories on the propulsion of a flapping airfoil in forward flight in terms of the Reynolds and Strouhal number. Phys. Rev. Fluids 6 (12), 123101.

Arranz, G., Flores, O., Garcia-Villalba, M., 2022a. Flow interaction of three-dimensional self-propelled flexible plates in tandem. J. Fluid Mech. 931.

Arranz, G., Martínez-Muriel, C., Flores, O., García-Villalba, M., 2022b. Fluid-structure interaction of multi-body systems: Methodology and applications. J. Fluids Struct. 110, 103519.

Arredondo-Galeana, A., Young, A.M., Smyth, A.S.M., Viola, I.M., 2021. Unsteady load mitigation through a passive trailing-edge flap. J. Fluids Struct. 106, 103352.

Bose, C., Sarkar, S., 2018. Investigating chaotic wake dynamics past a flapping airfoil and the role of vortex interactions behind the chaotic transition. Phys. Fluids 30 (4), 047101.

Bottasso, C.L., Croce, A., Gualdoni, F., Montinari, P., 2016a. Load mitigation for wind turbines by a passive aeroelastic device. J. Wind Eng. Ind. Aerodyn. 148, 57–69.

Bottasso, C.L., Croce, A., Gualdoni, F., Montinari, P., Riboldi, C.E.D., 2016b. Articulated blade tip devices for load alleviation on wind turbines. Wind. Energ. Sci. 1 (2), 297–310.

De Croon, G.C.H.E., De Clercq, K., Ruijsink, R., Remes, B., De Wagter, C., 2009. Design, aerodynamics, and vision-based control of the DelFly. Int. J. Micro Air Veh. 1 (2), 71–97.

Eldredge, J.D., Jones, A.R., 2019. Leading-edge vortices: mechanics and modeling. Annu. Rev. Fluid Mech. 51 (1), 75–104.

Felis, M.L., 2017. RBDL: An efficient rigid-body dynamics library using recursive algorithms. Auton. Robots 41 (2), 495–511.

Fernandez-Feria, R., 2016. Linearized propulsion theory of flapping airfoils revisited. Phys. Rev. Fluids 1 (8), 084502.

Fernandez-Feria, R., 2017. Note on optimum propulsion of heaving and pitching airfoils from linear potential theory. J. Fluid Mech. 826, 781–796.

Folkertsma, G.A., Straatman, W., Nijenhuis, N., Venner, C.H., Stramigioli, S., 2017. Robird: a robotic bird of prey. IEEE Robot. Autom. Mag. 24 (3), 22–29.

Gaitan-Aroca, J., Sierra, F., Castellanos Contreras, J.U., 2020. Bio-inspired rotor design characterization of a horizontal axis wind turbine. Energies 13 (14), 3515.

Garrick, I.E., 1936. Propulsion of a Flapping and Oscillating Airfoil. Tech. Rep., NACA Report 567.

Han, B., Zhou, L., Yang, F., Xiang, Z., 2016. Individual pitch controller based on fuzzy logic control for wind turbine load mitigation. IET Renew. Power Gener. 10 (5), 687–693.

Holden, J.R., Caley, T.M., Turner, M.G., 2015. Maple seed performance as a wind turbine. In: 53rd AIAA Aerospace Sciences Meeting. p. 1304.

Jeong, J., Hussain, F., 1995. On the identification of a vortex. J. Fluid Mech. 285, 69–99.

Johnson, S.J., Baker, J.P., Van Dam, C., Berg, D., 2010. An overview of active load control techniques for wind turbines with an emphasis on microtabs. Wind. Energy 13 (2–3), 239–253.

Jones, A.R., Cetiner, O., Smith, M.J., 2022. Physics and modeling of large flow disturbances: discrete gust encounters for modern air vehicles. Annu. Rev. Fluid Mech. 54 (1), 469–493.

Lackner, M.A., van Kuik, G., 2010. A comparison of smart rotor control approaches using trailing edge flaps and individual pitch control. Wind. Energy 13 (2–3), 117–134.

Marais, C., Thiria, B., Wesfreid, J.E., Godoy-Diana, R., 2012. Stabilizing effect of flexibility in the wake of a flapping foil. J. Fluid Mech. 710, 659–669.

Martínez-Muriel, C., Arranz, G., García-Villalba, M., Flores, O., 2023. Fluid-structure resonance in spanwise-flexible flapping wings. J. Fluid. Mech 964, A5.

Martínez-Muriel, C., Flores, O., 2020. Analysis of vortical gust impact on airfoils at low Reynolds number. J. Fluids Struct. 99, 103138.

Martínez-Muriel, C., García-Villalba, M., Flores, O., 2024a. On the role of wake-capture and resonance in spanwise-flexible flapping wings in tandem. J. Fluids Struct. 130, 104175.

Martínez-Muriel, C., Viola, I., Garcia-Villalba, M., Flores, O., 2024b. Mitigating Unsteady Loads at Low Reynolds Numbers Using a Passive Trailing-Edge Flap – Supplementary Material. Zenodo, http://dx.doi.org/10.5281/zenodo.14361440.

Moriche, M., 2017. A Numerical Study on the Aerodynamic Forces and the Wake Stability of Flapping Flight at Low Reynolds Number (Ph.D. thesis). Universidad Carlos III Madrid.

Moriche, M., Sedky, G., Jones, A.R., Flores, O., García-Villalba, M., 2021. Characterization of aerodynamic forces on wings in plunge maneuvers. AIAA J. 59 (2), 751–762.

Moulin, B., Karpel, M., 2007. Gust loads alleviation using special control surfaces. J. Aircr. 44 (1), 17–25.

Navalkar, S.T., Bernhammer, L.O., Sodja, J., van Solingen, E., van Kuik, G.A.M., van Wingerden, J.W., 2016. Wind tunnel tests with combined pitch and free-floating flap control: data-driven iterative feedforward controller tuning. Wind. Energy Sci. 1 (2), 205–220.

Otomo, S., Henne, S., Mulleners, K., Ramesh, K., Viola, I.M., 2021. Unsteady lift on a high-amplitude pitching aerofoil. Exp. Fluids 62 (1), 1–18.

Perrotta, G., Jones, A.R., 2018. Quasi-steady approximation of forces on flat plate due to large-amplitude plunging maneuvers. AIAA J. 56 (11), 4232–4242.

Roshanbin, A., Altartouri, H., Karásek, M., Preumont, A., 2017. COLIBRI: A hovering flapping twin-wing robot. Int. J. Micro Air Veh. 9 (4), 270–282.

Senda, K., Obara, T., Kitamura, M., Yokoyama, N., Hirai, N., Iima, M., 2012. Effects of structural flexibility of wings in flapping flight of butterfly. Bioinspir. Biomim. 7 (2), 025002.

Theodorsen, T., 1935. General Theory of Aerodynamic Instability and the Mechanism of Flutter. Tech. Rep., NACA Report 496.

Theodorsen, T., Garrick, I.E., 1942. Nonstationary Flow About a Wing-Aileron-Tab Combination Including Aerodynamic Balance. Tech. Rep., NACA Report 736.

Uhlmann, M., 2005. An immersed boundary method with direct forcing for the simulation of particulate flows. J. Comput. Phys. 209 (2), 448–476.

Viola, I.M., Bot, P., Riotte, M., 2013. On the uncertainty of CFD in sail aerodynamics. Internat. J. Numer. Methods Fluids 72 (11), 1146–1164.